ON-BODY CALIBRATION AND MEASUREMENTS USING A PERSONAL, DISTRIBUTED EXPOSIMETER FOR WIRELESS FIDELITY

Arno, Thielens[*], Sam, Agneessens[†], Hans, De Clercq[‡], Jeroen, Lecoutere[‡], Leen, Verloock[*], Emmeric, Tanghe[*], Sam, Aerts[*], Robert, Puers[‡], Hendrik, Rogier[†], Luc, Martens[*], and Wout, Joseph[*]

(email: arno.thielens@intec.ugent.be, tel: +32 9 33 14918, fax: +32 9 33 14899)

[*] **Wireless & Cable Group, Department of Information Technology, Ghent University / iMinds**

Gaston Crommenlaan 8, B-9050 Ghent, Belgium

[†] **Electromagnetics Group, Department of Information Technology, Ghent University**

Sint-Pietersnieuwstraat 41, B-9000 Ghent, Belgium

[‡] **Micro-electronics and Sensors, ESAT - MICAS, KULeuven**

Kasteelpark Arenberg 10 - bus 2443, B-3001 Leuven, Belgium

Funding - **Research Foundation Flanders (FWO-V); grant number: 3G004612. E. Tanghe is a Post-Doctoral Fellow of the FWO-V.**

Abstract- **This paper describes the design, calibration, and measurements with a personal, distributed exposimeter (PDE) for the on-body detection of radio frequency (RF) electromagnetic fields due to Wireless Fidelity (WiFi) networks. Numerical simulations show that using a combination of two RF nodes placed on the front and back of the body reduces the 50% prediction interval (PI_{50}) on the incident free-space electric-field strength (E_{RMS}^{free}). Median reductions of 10 dB and 9.1 dB are obtained compared to the PI_{50} of a single antenna placed on the body, using a weighted arithmetic and geometric average, respectively. Therefore, a simple PDE topology, based on two nodes, which are deployed on opposite sides of the human torso, is applied for calibration and measurements. The PDE is constructed using flexible, dual-polarized textile antennas and wearable electronics, which communicate wirelessly with a Universal Serial Bus (USB) connected receiver and can be unobtrusively integrated into garment. The calibration of the PDE in an anechoic chamber proves that the PI_{50} of the measured E_{RMS}^{free} is reduced to 3.2 dB. To demonstrate the real-life usability of the wireless device, a subject is equipped with the PDE during a walk in the city of Ghent, Belgium. Using a sample frequency of 2 Hz, an average incident power density of 59 nW/m² is registered in the WiFi frequency band, during this walk.**

Key Words- **Dosimetry; Radio frequency exposure; Textile antennas; PIFA; Wearable electronics**

I. INTRODUCTION

The number of sources that emit radio frequency (RF) electromagnetic radiation has considerably risen in the past decade. This increase in RF radiation is accompanied by an increasing number of studies (Frei et al., 2009; Joseph et al., 2008, 2010; Knafl et al., 2008; Neubauer et al., 2007; Roösli et al., 2008; Viel et al., 2009) that aim at quantifying exposure of the human body to RF radiation. This is motivated by the potential adverse health effects associated with this radiation. The physical quantity investigated in these studies, and also commonly considered in legislation and standardization, is the RF electric-field strength or power density incident on the human body (ICNIRP, 1998).

A principal frequency band for wireless communication, generating RF radiation, is the Wireless Fidelity (WiFi) communication band. This band is particularly exploited (Cisco, 2013) for wireless communication with personal RF devices. Therefore, it is necessary to assess the personal exposure to WiFi signals, preferably using a measurement device with a low measurement uncertainty. An individual's personal exposure to RF electromagnetic radiation is typically measured using Personal Exposimeters (PEMs). These are on-body worn devices that measure the electric-field strengths on the same location and time as the subject wearing the device. However, PEMs are faced with relatively large measurement uncertainties (Neubauer et al., 2010; Bolte et al., 2011; Iskra et al., 2011), mainly caused by the influence of the body on the measurements using PEMs. Another problem is that these devices have a significant crosstalk, being the power that is emitted in a certain band and registered in another, which perturbs the data recorded by PEMs (Thielens et al., 2014).

A possible approach to reduce these uncertainties is the use of multiple antennas distributed on the body. To this aim, a personal, distributed exposimeter (PDE) is proposed in Thielens et

al. 2013a. This device consists of multiple antennas placed on the human body. The PDE is calibrated on a male subject in an anechoic chamber using textile antennas (Agneessens et al., 2012) and wearable electronics (Jourand et al., 2010). A wired prototype of the PDE demonstrates that a calibration on a subject wearing the PDE can reduce the uncertainty on measurements of the incident power densities (or electric-field strengths) drastically (Thielens et al., 2013a). However, the interconnections using wires make the proposed prototype of the PDE unsuitable for measurements outside the laboratory. Wireless interconnections between the antennas are necessary in order to use the PDE during measurements in real-life situations. The previously proposed PDE measures in the Global System for Mobile Communication (GSM) around 900 MHz (GSM900) bands and cannot be used for the detection of WiFi. A PDE thus has to be developed specifically for WiFi. Another drawback in the previously proposed PDE is the use of linearly polarized patch antennas (Thielens et al., 2013a). Deviations in the orientation of the antennas' polarization are inevitable when positioning the antennas on the body. A solution to this problem is to use dual-polarized patch antennas that record the projection of the electric field on the antenna's surface.

The goal of this study is to design, for the first time, a *wireless* PDE that measures personal exposure to RF fields originating from WiFi networks. The PDE is constructed using dual-polarized textile antennas, wireless interconnections, and wearable electronics. This design allows us to perform measurements using the PDE in a real (sub)urban environment, after calibration in an anechoic chamber. The goal of the measurement device is to assess one's personal exposure with less uncertainty. These kinds of measurements are used in exposure assessment and epidemiological studies that study possible health effects of exposure to RF radiation.

II. MATERIALS AND METHOD

Numerical simulations using a heterogeneous human body phantom are executed to demonstrate that a combination of two WiFi antennas reduces the uncertainty of measurements of the incident power density or electric-field strength. A PDE is then designed, with two antennas placed on the body. Textile antennas and wearable electronics are designed and constructed for the appropriate frequency band: WiFi at 2.45 GHz (2400-2483.5 MHz). A calibration of the PDE is carried out in the anechoic chamber. Afterwards this calibration is used to process measurement results in a realistic environment.

A. Textile antennas

The RF radiation in the WiFi band is measured using a dual-polarized patch antenna. Dual polarization enables one to capture two orthogonal components of the RF fields with one antenna, making antenna orientation with respect to the human body less critical. This antenna operates at half-wavelength length (approximate dimensions (WxLxH): 7 cm x 7 cm x 0.4 cm) and is fabricated from textile materials to ensure wearability. The conductive parts are made from copper plated nylon (conductivity = 0.18 Ω/sq), while the antenna substrate is a closed-cell expanded-rubber (ϵ_r = 1.49, tan δ = 0.016). The bandwidth is 5.1%, the radiation efficiency 66%, and the maximal gain 6.7 dBi. Fig. 1 shows the magnitude of the measured power reflection coefficient ($|S_{11}|$) of the textile antenna around the frequencies of interest. Two textile antennas are fabricated for this study.

B. Wireless Interconnections and Wearable Electronics

Each textile antenna is extended with an RF-exposure acquisition node. The nodes contain a commercially available receiver that is tuned for a 2450 MHz link (CC2500, Texas Instruments, Dallas, TX, USA) and a microcontroller (CC430F5137, Texas Instruments,

Dallas, TX, USA) for data management. RF-exposure data is communicated via a 433 MHz wireless link, with an input power of -6 dBm, to an off-body unit that interfaces with a personal computer using Universal Serial Bus (USB). A modular architecture is adopted, such that the amount of nodes is easily extendable and other frequency bands can be explored. Acquisition parameters, such as the sample rate and the frequency channel, can be adjusted during the experiment to optimize the acquired data. Instead of sampling the full spectrum of the measured band at once, an adjustable filter is added in order to be able to sweep the full spectrum using more narrow bands, achieving a high frequency resolution. The maximum value measured in each frequency sweep is saved. This version of the PDE is designed with minute attention to power optimization and the on-body wireless communication link. The RF nodes have a sensitivity of -90.5 ± 0.5 dBm with a dynamic range of 100 dB.

C. Numerical Simulations

The goal of the simulations is to demonstrate that the incident power density in the WiFi band can be estimated with a smaller uncertainty using a PDE consisting of 2 nodes instead of existing PEMs.

To this aim, Finite-Difference Time-Domain (FDTD) simulations using the Virtual Family Male (VFM) (Christ et al., 2010) (grid step = 1.5 mm) are executed. The VFM is a heterogeneous human body model consisting of 81 different tissues with a BMI (body mass index) of 22.3 kg/m². The dielectric properties assigned to the phantom's tissues are taken from the Gabriel database (Gabriel et al., 1996). FDTD is usually used to determine the electric fields inside a phantom (Vermeeren et al., 2008, 2013; Thielens et al., 2013), but the electric fields surrounding the phantom can be obtained from those simulations as well. A method to determine these electric fields for realistic exposure scenarios is presented in

Vermeeren et al. 2008 and confirmed in Iskra et al. 2011, Vermeeren et al. 2013, and Thielens et al. 2013a, 2013b. In summary, the method performs FDTD simulations of the VFM under exposure of single plane waves and combines those in order to emulate realistic exposure scenarios. A stochastic approach is then used to determine the exposure in realistic environments. The same method is used in this study to estimate the electric fields surrounding the VFM at 2450 MHz, the 'center' frequency of the WiFi band. The environment used for a study of realistic exposure is the 'Indoor Pico-cell' scenario (Thielens et al., 2013b; Vermeeren et al., 2013). The effect of combining different measurement nodes on the body is investigated using these numerical simulations.

First, the electric fields at 1 cm (height antennas + 0.6 cm for a connector located at the back of the antennas) from the phantom's torso (upper body without head and arms) are determined by means of numerical simulations, which are executed at 2450 MHz. In a previous study, all positions at 1 cm from the phantom's upper body (except the face) were allowed as possible locations to deploy antennas (Thielens et al., 2013a). Yet, it is unrealistic to expect stable measurements from antennas placed on the head and limbs, due to the movement of those body parts during measurements. Therefore, those positions are not allowed in this study, as the authors also aim at measuring in real environments. The grid-cells at 1 cm from the upper-body can be unrealistically close to one another, since the grid step will be close to 1.5 mm at 1 cm from the body. Therefore, a discretization in the azimuth angle φ of 10° and another discretization along the Z coordinate (being in the direction of the body's main axis) of 10 cm are introduced. This reduces the number of potential locations to deploy antennas to N_{cell} = 187. The locations are then divided into two groups: front of the torso (103 points) and back of

the torso (84 points). Fig. 2 shows these potential locations to deploy antennas as blue circles (front) and red circles (back).

Second, the electric fields are determined in the N_{cell} possible locations to deploy antennas for realistic exposure samples, taking into account the antenna polarization. As mentioned before, the WiFi-band antennas are dual polarized. Therefore, the projection of the electric fields in the tangential plane to the human body is studied, instead of the full electric field vector. The field strength of this projection is denoted $E_{RMS,j}^{body}$, with j= 1…N_{cell}. The quantity studied is the response of the exposimeter R_j, which is the quadratic ratio of the electric-field strengths recorded by the node on position *j*: $E_{RMS,j}^{body}$ (the quantity one *can* measure) and the incident root-mean-squared (RMS) electric fields E_{RMS}^{free} (the quantity one *wants* to know for exposure assessment purposes):

$$R_j = \left(\frac{E_{RMS,j}^{body}}{E_{RMS}^{free}} \right)^2 \quad (1)$$

For every possible location on the body j (j =1…N_{cell}), R_j is determined in 5000 realistic exposure samples, resulting in a distribution of R_j. Each of these j distributions has an interquartile distance (D_j), being the difference between the 75% and 25% percentile of R_j.

Third, combinations of two different antennas are investigated. One antenna is placed on the front of the body and one on the back of the body. In this case the electric fields recorded by the nodes are averaged over both nodes on the body. The weighted arithmetic (R_{av}) and geometric (R_{geom}) averaged responses are then defined as:

$$R_{av,l}(w) = \frac{w\left(E_{RMS,front,l}^{body}\right)^2 + (1-w)\left(E_{RMS,back,l}^{body}\right)^2}{\left(E_{RMS}^{free}\right)^2} \quad (2)$$

$$R_{geom,l}(w) = \frac{\left(\mathrm{E}^{\mathrm{body}}_{\mathrm{RMS,front,l}}\right)^{2\times w} \times \left(\mathrm{E}^{\mathrm{body}}_{\mathrm{RMS,back,l}}\right)^{2\times(1-w)}}{\left(\mathrm{E}^{\mathrm{free}}_{\mathrm{RMS}}\right)^{2}} \quad (3)$$

with $\mathrm{E}^{\mathrm{body}}_{\mathrm{RMS,front,l}}$ and $\mathrm{E}^{\mathrm{body}}_{\mathrm{RMS,back,l}}$ the l^{th} combination of two antennas on the body and the weight $w \in [0,1]$. For every combination of two antennas (l) and weight w, values $R_{av,l}(w)$ and $R_{geom,l}(w)$ are determined in 5000 realistic exposure samples, resulting in distributions of $R_{av,l}(w)$ and $R_{geom,l}(w)$. The interquartile distances ($D_{av,l}(w)$ and $D_{geom,l}(w)$) are determined for every $w \in [0,1]$. The distributions of these interquartile distances are then compared to those of single measurement points in order to show the advantage of a (weighted) averaging over two nodes.

D. Setup in the Anechoic Chamber

The calibration measurements are executed using the same setup as in Bolte et al. 2011, Thielens et al. 2013a, and 2014. The calibration is executed in an anechoic chamber, which is designed to provide damping of the reflected signals for the frequency band studied in this paper. A WR-430 standard gain horn (being a linearly polarized transmitting horn antenna, TX) with a reflection coefficient smaller than -10 dB in the studied frequency band is used as source. This TX is fed by a network analyzer, Agilent N5242A PNA-X (Agilent, Santa Clara, CA, USA). The network analyzer delivers a signal at 2450 MHz with a bandwidth of 1 Hz at a constant input power of 10 mW to the TX, which is placed in the far field of a rotation platform on the other side of the anechoic chamber. In this study, two orthogonal polarizations of the TX are studied: a vertical polarization (V) parallel to the rotational platforms axis of rotation and a horizontal polarization (H) perpendicular to this axis of rotation.

Two steps are performed in the calibration: First, the incident electric fields are measured in free space using a broadband field meter (Narda NBM-550, Narda Microwave, Hauppauge, NY, USA). Second, on-body measurements using the PDE are executed.

The goal of measurements with the PDE is to determine the incident electric field strength. This field strength is to be averaged over the human body (ICNIRP, 1998). In the first calibration step the incident (free-space) electric field is measured at different heights (0.5 m to 2 m) of the rotational axis above the platform. Since the subject is placed on the platform, this is the rotational axis of the subject as well. The free-space incident electric field (E_{RMS}^{free}) is determined as an average over these measured incident electric fields ($E_{RMS}(h)$) using:

$$E_{RMS}^{free} = \sqrt{\frac{1}{N_h}\sum_{i=1}^{N_h} E_{RMS}^2(h_i)} \tag{4}$$

where N_h is the number of measured heights h_i along the rotational axis from 0.5 m to h_{tot}, being the subject's total body height. The incident power density $S_{inc}^{free} = \frac{E_{RMS}^{free\,2}}{377\ \Omega}$.

In the second step of the calibration, a 25 year old male subject wearing the PDE is placed on the rotation platform in the anechoic chamber. As shown further in this manuscript, any combination of two nodes on the front and the back reduces the uncertainty on measurements of the incident electric field. For their measurements, the authors have chosen to work with the positions indicated in Fig. 2. The subject has a body mass index of 22.8 kg/m², a h_{tot} of 1.91 m, and a mass of 83 kg.

Two types of on-body measurements are carried out. First, the subject is rotated over 360° in azimuth (φ), in order to emulate a random orientation regarding azimuth in a real

environment, for a constant transmitted power at 2450 MHz using both H and V polarization. During the rotation, the received power ($P_{r,i}(\varphi)$) on antenna *i* (*i* = 1, 2; Fig. 2) is recorded as a function of the azimuth angle φ. Second, the subject is stationary, facing the TX, and the power at the TX (P_{in}) is varied. During this power sweep, the received powers on the antennas are recorded ($P_{r,i}(P_{in})$). This is necessary to determine an on-body detection limit.

Using calibration data to process measurements in a real environment

During measurements in a real environment, a power ($P_{r,i}^{meas}$) is received on each antenna *i* (*i* = 1, 2; Fig.2). The incident power density (S_{inc}) is determined from this received power using:

$$S_{inc} = \frac{P_{r,i}^{meas}}{AA_i} \tag{5}$$

where AA_i (m²) is the effective median on-body antenna aperture. During the calibration, the received powers ($P_{r,i}(\varphi)$), on the different antennas *i* of the PDE, are registered while rotating a subject, equipped with the PDE, in the anechoic chamber under exposure of RF radiation emitted by the H or V polarized TX at a constant input power P_{in}. The free-space incident power densities $S_{inc}^{free,H}$ and $S_{inc}^{free,V}$ are determined for these same polarizations and input power using eqn (4). The antenna apertures for the H and V polarization, AA_i^H and AA_i^V, are determined using:

$$AA_i^{H/V}(\varphi) = \frac{P_{r,i}^{H/V}(\varphi)}{S_{inc}^{free,H/V}} \tag{6}$$

Eqn (5) requires AA_i values for an unknown polarization but the calibration measurements are conducted for two orthogonal polarizations H and V, eqn (6). However, the incident electric field $\bar{E}_{RMS}^{free}$ can be written as a sum of two orthogonal components:

$$\bar{E}^{free} = E_H \times \bar{1}^H + E_V \times \bar{1}^V = \left|\bar{E}^{free}\right|(\cos(\psi)\,\bar{1}^H + \sin(\psi)\,\bar{1}^V) \tag{7}$$

with $\bar{1}^H$ and $\bar{1}^V$ the unity vectors in the horizontal and vertical directions, and ψ the polarization. A Gaussian distribution for the polarization ψ has been proposed in Olivier 2002 and Kalliola et al. 2002, and used in Vermeeren et al. 2008, 2013, Iskra et al. 2011, and Thielens et al. 2013b. This distribution is applicable for communication signals emitted from base stations located outdoor that cover large areas using an array of linearly (or cross) polarized antennas. For WiFi signals, a uniform distribution for $\psi \in [0,2\pi]$ is used, since no a priori assumptions can be made about the polarization for WiFi sources. Eqn (5) is rewritten as:

$$P_{r,i}^{meas}(\varphi,\psi) = AA_i(\varphi,\psi) \times S_{inc} \tag{8}$$

This is reformulated using eqn (7):

$$\begin{aligned} P_{r,i}^{meas}(\varphi,\psi) &= AA_i^V(\varphi)S_{inc}^V + AA_i^H(\varphi)S_{inc}^H \\ &= (AA_i^H(\varphi)\,cos^2(\psi) + AA_i^V(\varphi)\,sin^2(\psi))S_{inc} \end{aligned} \tag{9}$$

with $AA_i^{V/H}$ the antenna aperture for vertically (S_{inc}^V) or horizontally (S_{inc}^H) polarized incident power densities. From eqns (8) and (9), an expression for AA_i is obtained:

$$AA_i(\varphi,\psi) = AA_i^H(\varphi)\,cos^2(\psi) + AA_i^V(\varphi)\,sin^2(\psi) \tag{10}$$

This formula is calculated for every (φ, ψ) pair, resulting in a distribution of $AA_i(\varphi, \psi)$ for every antenna i. In Bolte et al. 2011 this distribution was assumed to be U-shaped and thus symmetric, which would allow one to describe the distribution using a median or mean value, and a standard deviation or half the interquartile distance to characterize the distribution. However, it has been shown in Thielens et al. 2013a and 2014, that depending on the antenna's position, this distribution is asymmetric and is, therefore, better described using three quartiles: $Q_{1,i}$, $Q_{2,i}$, and $Q_{3,i}$, being the 25%, 50%, and 75% percentiles of the antenna aperture of antenna i, respectively. The quartiles are used to determine relative upper (u_{up}) and lower (u_{low}) limits of the 50% prediction interval, caused by the presence of the body, on S_{inc}:

$$u_{up} = \frac{Q_{2,i}}{Q_{1,i}} - 1 \tag{11}$$

$$u_{low} = 1 - \frac{Q_{2,i}}{Q_{3,i}} \tag{12}$$

The goal of the PDE is to combine N different antennas in order to reduce the variation on the data, i.e., the 50% prediction interval on measured data. In practice, the received power during the calibration will be averaged over N different antennas:

$$P_r^{av} = \sum_{i=1}^{N} w_i P_{r,i} \quad with \quad \sum_{i=1}^{N} w_i = 1 \tag{13}$$

$$P_r^{geom} = \prod_{i=1}^{N} {P_{r,i}}^{w_i} \quad with \quad \sum_{i=1}^{N} w_i = 1 \tag{14}$$

with P_r^{av}, the weighted, arithmetic averaged received power; P_r^{geom} the weighted, geometric averaged received power; and w_i weight coefficients for the individual received powers. P_r^{av} and P_r^{geom} can be used to determine averaged antenna apertures AA^{av} and AA^{geom} with their own distribution and their own quartiles $Q_1^{av/geom}$, $Q_2^{av/geom}$, and $Q_3^{av/geom}$. These quantities can be inserted into eqns (11) and (12), in order to determine a 50% prediction interval on the power density ($S_{inc}^{av/geom}$) associated with $P_r^{av/geom}$. The weight coefficients w_i could be chosen equal to 1/N, to obtain regular arithmetic or geometric averages, as proposed in Thielens et al. (2013a).

F. Measurements in a real environment

The subject, equipped with the PDE, follows a predefined walk in Ghent, Belgium, shown in Fig. 3. The walk is performed on a weekday during business hours in the afternoon (12h-16h) and is approximately 1.9 km long. The buildings along the route are mainly residential buildings of 3 to 4 stories high, some of the ground floors are used for commercial purposes. The PDE records received powers with a sample rate of 2 Hz. The same path is followed twice during the same afternoon, in order to increase the number of measured samples.

The RF nodes connected to the antennas record the received power on the antennas. These nodes have a certain detection limit in terms of received power and thus power density, which implies that if a received power, equal to this detection limit is registered, the actual received power might be lower than or equal to this value. This left-censored data might lead to an overestimation of summary statistics of RF power densities (Helsel et al., 2005; Röösli et al., 2008). A commonly used technique to process left-censored data is Robust Regression on Order Statistics (ROS) in which a lognormal distribution is fitted to the (probability) of the

data above the detection limit. Censored data is then replaced by data lower or equal to the detection limit from the lognormal distribution (Bolte et al., 2012; Joseph et al., 2010; Röösli et al., 2008). This technique can only be applied if a sufficient amount (>20%) of data is recorded above the detection limit (Helsel et al., 2005; Röösli et al., 2008). When necessary, the same technique is used to process the data measured in this study. For the dual-polarized WiFi antennas, ROS has to be applied to the separate data registered for each polarization of the antennas. If ROS has to be applied, it has to be applied before any averaging takes place using eqns (13) or (14).

During the walk, 2 EME SPY 140 (Satimo, Brest, France) PEMs are worn on both hips of the subject. These PEMs measure with a sample rate of 0.25 Hz. The values measured by the PEMs can be used for comparison with the values measured with the PDE. The data measured using the PEMs is first processed using ROS and then averaged over both hips using eqn (13) with $w_i = 1/2$. The data is also corrected for the presence of the human body using the techniques described in Bolte et al. (2011) and applied in Thielens et al. (2014) for a combination of 2 PEMs and realistic polarizations.

III. RESULTS

A. Numerical Simulations

5000 exposure samples of the VFM are simulated in the ’Indoor Pico-cell’ scenario (Vermeeren et al., 2008, 2013; Thielens et al., 2013b). This sample size is associated with an average value of the 95% confidence interval smaller than 16% for the response percentiles between 1% and 99%.

Fig. 4 shows the Experimental Cumulative Distribution Function (ECDF) of the interquartile distances D_j of the responses R_j of a single antenna placed on the N_{cell} possible locations shown in Fig. 2 and of combinations of a textile antenna placed on the front (F) and back (B) of the body. The averages are calculated using eqns (2) and (3). The curves denoted 'F & B arithmetic' and 'F & B geometric' are the distributions of the $D_{av,l}(\frac{1}{2})$ and $D_{geom,l}(\frac{1}{2})$ for averages where $w = 1/2$, while the curves denoted 'F & B arithmetic weights' and 'F & B geometric weights' are the distributions of $D_{av,l}(w)$ and $D_{geom,l}(w)$ for the weight coefficient $w \in [0,1]$ which corresponds to the lowest $D_{av,l}(w)$ or $D_{geom,l}(w)$ for combination l. w is determined with a resolution of 0.1.

Averaging over two antennas clearly reduces the interquartile distance of the distribution of the responses in a realistic environment: the ECDFs of $D_{av,l}(w)$ and $D_{geom,l}(w)$ are located at considerably smaller values than the ECDF for the single antenna interquartile distance. For a single antenna on the body, the median D_j is 14.9 dB, while, for a standard arithmetic and geometric average ($w = 1/2$), the median values of $D_{av,l}(\frac{1}{2})$ and $D_{geom,l}(\frac{1}{2})$ are 5.2 dB and 6.0 dB. This corresponds to a median reduction of 9.7 dB and 8.9 dB, for standard arithmetic and geometric averaging, respectively.

Given a certain set of electric fields $E^{body}_{RMS,front,l}$ and $E^{body}_{RMS,back,l}$, there exists a weight coefficient w, that is associated with an interquartile distance $D_{av,l}(w)$ or $D_{geom,l}(w)$, which is lower than or equal to the corresponding regular arithmetic or geometric averages $D_{av,l}(\frac{1}{2})$ or $D_{geom,l}(\frac{1}{2})$ ($w = 1/2$, in eqns (2) and (3)). This explains why the curves corresponding to the weighted averages are located at lower values for the interquartile distances than the

regular averages in Fig. 4. The median values are 4.9 dB and 5.8 dB, using the best weighted arithmetic and geometric average, respectively. The further reduction in interquartile distance when using a weighted average is small, 0.3 dB and 0.2 dB, for arithmetic and geometric averaging, respectively, compared to the reductions obtained when adding a second antenna on the other side of the body to a single antenna and taking a regular average. Nevertheless, a weighted average will be used in the calibration measurements, since it intrinsically provides a lower interquartile distance on the response and, thus, a lower measurement uncertainty caused by the presence of the body.

The best single antenna position on the body found using these simulations yields an interquartile distance of 8.6 dB. This interquartile distance is larger than any of the values found for an average of two nodes placed on the front and back of the body, using a weighted arithmetic average. Thus, for every combination of two antennas placed on the front and back of the upper torso, a weight factor w can be found such that an arithmetic or geometric average, using eqns (2) and (3), leads to a lower interquartile distance than can be obtained using a single antenna.

B. Calibration of the PDE

In a first step, the incident fields are measured. The measured incident electric-fields strengths at 2450 MHz for an input power of 10 mW at the input of the transmitting antenna are 0.12 V/m, for a horizontally polarized antenna, and 0.13 V/m, for a vertically polarized transmitting antenna.

In a second step, the on-body antennas, placed on the front and back, as indicated in Fig. 2, are calibrated. The power response of the PDE is linear. The detection limit of the RF nodes is -90.5 ± 0.5 dBm for the individual arms of the dual-polarized antenna attached to the WiFi

nodes. The powers $P_{r,i}^{H/V}(\varphi)$ are registered in steps $\Delta\varphi = 45°$ during the calibration for both H and V polarization. Multiple samples are recorded at every step in angle φ. The antenna apertures AA_i are calculated using these powers $P_{r,i}^{H/V}(\varphi)$ and the measured incident power densities S_{inc}^{free} using eqn (6). Afterwards, the antenna apertures AA_i are recalculated for a realistic polarization ψ, using eqn (10). To this aim, a bootstrap approach is implemented, where, in every repetition of the analysis, 10^3 ψ-samples are generated (see Materials and Methods section D) for every measured value. This number of ψ-samples is associated with an uncertainty on the summary statistics $Q_k^{av/geom}$ (k=1,2,3) smaller than 1% (determined using 100 bootstrap samples). The received powers are then averaged using weight coefficients $w_i \in [0,1]$ (with a resolution of 10^{-2}) under the constraints indicated in eqns (13) and (14). This is repeated during 100 bootstrap iterations. For every bootstrap sample (every set of 10^3 ψ samples), the quartiles of the antenna aperture $Q_k^{av/geom}$ are stored, together with the weights that correspond to the lowest interquartile distance. The median of the stored quantities is then determined from this set of quartiles, weights, and interquartile distances.

Table 1 lists the weight factors that yield the lowest interquartile distance for a realistic polarization, together with the determined AA_i. Fig. 5 shows the corresponding interquartile distances. From Fig. 5, it is clear that using a weighted average of the power received by multiple antennas, positioned intelligently on the body, reduces the variation caused by the presence of the body (here quantified by the 50% prediction interval) on measurements using these antennas. At 2450 MHz, the interquartile distance is reduced down to 3.2 dB using two cross-polarized antennas. As Fig. 5 shows, this interquartile distance is lowest for geometric

averaging. This averaging scheme is, therefore, used during the measurements in a real environment.

Applying the antenna apertures and weights listed in Table 1, the detection limits for the received powers (dBm) are converted to values in power density (W/m²). The detection limits in the WiFi band range from 0.9 to 7.4 x 10^{-9} W/m². The detection limit of the PDE in the WiFi band is about 10 times lower than that of a commercial exposimeter O(10^{-8} W/m²).

C. Measurements in Ghent

Table 2 lists the summary statistics of the measurements during a walk in Ghent, described in Fig. 3. Due to the low detection limit of the RF nodes, the number of censored samples is relatively low (up to 0.8% in Table 2), compared to those of commercial exposimeters, which may be higher than 80% (Röösli et al., 2008). The mean value and the quartiles measured by the individual nodes, and the combination of two antennas with the smallest interquartile distance, found in the calibration (geometric averaging, Fig. 5), using the weights listed in Table 1, are listed in Table 2 for WiFi.

IV. DISCUSSION

A. Numerical Simulations

The results of the numerical simulations shown in Fig. 4 indicate that a (weighted) average over two antennas on the front and back of the upper torso does reduce the interquartile distance on the simulated response: 10 dB and 9.1 dB reductions on the median interquartile distance of the response of the PDE, using a weighted arithmetic and geometric average. The simulations also show that the exact positions of the antennas are not that critical for the value of the interquartile distance: 95% of all studied combinations of two antennas yield an interquartile distance within an interval of 2.1 dB and 2.4 dB, for a weighted arithmetic and

geometric average, respectively. Moreover, as Fig. 4 shows, any combination of two textile antennas placed on the front and back of the torso leads to a lower interquartile distance than obtained by a single antenna.

In Iskra et al. 2011, numerical simulations with an adult human body model are performed to investigate the variation of the response of a single and a dual PEM (one PEM on both front and back of the torso) in different fading scenarios. The mean values of the 95% prediction interval (the ratio of the 97.5% and 2.5% percentiles) over different (combinations of) positions of isotropic PEMs on the front and back of the body are 25.6 dB for a single PEM and 10.8 dB for a combination of two PEMs at 2100 MHz. The simulations in the current study (at 2450 MHz) result in a mean 95% prediction interval of 33.8 dB for single textile antennas and 14.5 dB for a combination of two textile antennas placed on the front and the back of the torso. The values found in this study are larger because of the higher frequency, which causes more variation of the electric fields near the body (Iskra et al., 2011) and the fact that the textile antennas can only record a projection of the electric field instead of the full vector, which also increases the variation (Thielens et al., 2013a). In Neubauer et al 2010, the variation of the response of a single PEM was investigated near the body of another male phantom placed in a model for a real indoor environment. A 50% prediction interval of 9.6 dB (versus 14.8 dB found in this manuscript) was found at 2450 MHz for 10 potential locations of the PEM on the body, including locations on the hips and arms, which are not included in the current study. The higher variation in this study can be attributed to the fact that, in Neubauer et al. 2010, the full electric field vectors were considered and averaged over a larger volume, while in this study the projection of the electric field in a point is considered.

The studied interquartile distances and prediction intervals could depend on the used phantom or frequency. This dependency is studied in Iskra et al. 2011, where both an adult and child phantom are simulated at three different frequencies: 450, 900, and 2100 MHz. The differences in average responses over all considered positions on the torso of the adult and child model are smaller than 4%. The average responses increase with frequency for both phantoms in Iskra et al. 2011 and the variation on the responses increases with frequency as well. In Neubauer et al. 2010, the average responses and variations on those responses were studied at 4 frequencies: 100, 946, 2140, and 2450 MHz. Differences between the average responses and their variation are observed in Neubauer et al. 2010. However, the same frequency dependence as observed in Iskra et al. 2011 was not found. These findings confirm that variations of the prediction interval with used frequency or phantom do exist. The numerical simulations presented in this study could be repeated for other phantoms at other frequencies, in order to study this dependency.

B. Calibration of the PDE

As Fig. 5 shows, the improvements using weight coefficients and averaging over multiple antennas can be relatively large. For the WiFi (2450 MHz) band, the single antenna with the lowest interquartile distance has an interquartile distance of 17 dB, which can be reduced considerably using geometric averaging to 3 dB. This interquartile distance is small compared to previous studies (Neubauer et al., 2010; Bolte et al., 2011; Thielens et al., 2013). In Neubauer et al. 2010, the variation of the response of a single PEM was investigated near the body of a phantom, placed in a model for a real indoor environment. A 50% prediction interval of 9.6 dB was obtained at 2450 MHz. In Bolte et al. 2011, an exposimeter was worn on the hip of a male subject. This exposimeter was calibrated using the same procedure described here in

this study. However, only two polarizations were considered. 50% prediction intervals of 9 dB and 19 dB were measured in the WiFi band, for horizontal and vertical polarization, respectively. In Thielens et al. 2013a a 50% prediction interval of 4.5 dB for a prototype of a PDE at 950 MHz was measured for both incident polarizations using the same calibration procedure, without weight factors however. All previously mentioned 50% prediction interval values are larger than 3 dB, which indicates that the proposed calibration method will reduce the variation on the measurements. Moreover, it should be noted, that, in contrast to existing portable solutions, the system proposed here is fully wearable and that it may be comfortably and unobtrusively integrated into a garment. Our system is, therefore, completely invisible and it does not hinder the movements not the behaviour of the wearer.

C. Measurements in Ghent

Measurements of the WiFi signals are executed along an outdoor trajectory in the city center of Ghent (Belgium, Fig. 1). These measurements are performed by a subject who is simultaneously equipped with the PDE described in this manuscript and a combination of 2 (commercial) PEMs (Satimo, Brest, France) worn on both hips of the subject.

Table 2 lists the power densities measured using the PDE and those measured by the PEMs from Thielens et al. 2014. All values measured are lower than the reference levels issued by the international commission on non-ionizing radiation protection (ICNIRP) (ICNIRP, 1998). An average power density of 59 nW/m² is registered for WiFi signals with a 50% prediction interval defined by u_{low} = 32%, and u_{up} = 43%. This power density value is relatively low, compared to values measured indoor (Verloock et al., 2010): 38 μW/m² on average measured in an office environment. WiFi is predominantly emitted indoor and thus much weaker when measured outdoor due to penetration (and propagation) losses. The power density values

measured in the WiFi band are lower than those measured by the combination of 2 PEMs. This difference is attributed to the averaging scheme used by the EME SPY 140, where the maximum value is registered every 4 seconds. If the maximum of the data found in this study is calculated every 8 samples (4 s), then the values measured by the PDE become comparable to those measured by the commercial exposimeters: for example, the mean values are 0.35, 0.14, and 0.52 μW/m² for node 1, node 2, and the combination of the 2 nodes after calculating the maximum over 4 s. This is in excellent agreement with the measurements done with the PEMs, given the uncertainties listed in Table 2.

D. Future Research

A potential extension of the PDE for WiFi consists of adding more RF nodes on the body. However, as Thielens et al. 2013a suggest, the relative reduction in variation on measurements using the PDE decreases as a function of the number of used antennas. Moreover, the interquartile distance of the PDE is already of the same order of magnitude as the uncertainty on the free-space measurements of the incident power density (CENELEC, 2008). However, some further reductions in uncertainty are possible: the design could be improved by solving the O($C_{N_{cell}}^{N}$) problem where all possible locations are considered.

Another challenge consists of including more frequency bands in the PDE. The placement of a first band will influence the measurement uncertainty of the next band, because certain positions are not available anymore. An algorithm will be developed that takes this order of placement into account and searches for an optimal order of placement of the different antennas.

The calibration can be improved by including elevation and using real signals as applied in Lauer et al. 2012. The calibration can also be repeated for multiple subjects to determine the variability of the determined prediction intervals as a function of body morphology.

For the further enhancement of the system's wearability, research should be performed on integrating active circuitry onto the textile antennas. Also using multi-band antennas can help reducing the number of nodes, which improves the user's comfort.

V. CONCLUSIONS

A personal, distributed exposimeter (PDE) for the detection of Wireless Fidelity (WiFi) around 2450 MHz is calibrated and used for measurements in a real environment. Numerical simulations are performed to demonstrate that a combination of two textile antennas on the body reduces the uncertainty caused by the presence of the body on measurements of the incident electric-field strengths. A combination of two antennas, placed on the front and back of the body, has a smaller interquartile distance in terms of response on the incident electric-field strength than the interquartile distance of the response of the best single antenna placed on the on-body positions, considered in this study. The median reductions for this interquartile distance are 10 dB and 9.1 dB, using a weighted arithmetic and geometric average, respectively. The PDE is constructed using flexible textile antennas and wearable electronics, which can both be integrated in clothing, do not impede movement of a subject wearing the PDE, and communicate wirelessly with a receiver on a laptop, personal computer or personal device. Therefore, the PDE can be made invisible for other humans and will not alter a subject’s behavior while performing measurements. A calibration of the wireless PDE shows that the uncertainty in terms of the 50% prediction interval of the measured incident electric-

field strength can be significantly reduced to a minimal value of 3.2 dB for WiFi signals, respectively. This value is low in comparison with state-of-the-art personal exposimeters and a previous prototype of the PDE. In this way, one obtains lower uncertainties on measurements of the incident electric-field strength, calculated using these 50% prediction intervals. In addition, the on-body antenna factor of the weighted average of the different radio frequency (RF) nodes in the PDE is determined from the calibration. It is used to process received powers on those RF nodes registered during a walk in Ghent, Belgium. An average incident power density of 59 nW/m² is registered for RF fields originating from WiFi outdoor in an urban environment, recorded with a sample frequency of 2 Hz. All measured power densities are lower than the reference levels issued by ICNIRP.

FUNDING

Research Foundation—Flanders (FWO-V); grant number: 3G004612

ACKNOWLEDGEMENTS

E. Tanghe is a Post-Doctoral Fellow of the FWO-V (Research Foundation–Flanders). This research was partially funded by the Inter-University Attraction Poles Program initiated by the Belgian Science Policy Office.

REFERENCES

Bolte J.F.B., Van der Zande G., Kamer J. Calibration and uncertainties in personal exposure measurements of radiofrequency electromagnetic fields. Bioelectromagnetics 32(8): 652-663; 2011.

Bolte JFB, Eikelboom T. Personal radiofrequency electromagnetic field measurements in the Netherlands: Exposure level and variability for everyday activities, times of day and types of area. Environment International 48: 133-142; 2012.

CENELEC. European Committee for Eletrotechnical Standardisation TC 106x W1 EN 50492 in situ. Basic standard for the in-situ measurement of electromagnetic field strength related to human exposure in the vicinity of base stations. Brussels, Belgium; 2008.

CISCO, Cisco Visual Networking Index: Global Mobile Data Traffic Forecast Update, 2012–2017. White paper, February 2013; 2013.

Frei P, Mohler E. Neubauer G, Theis G, Burgi A, Frohlich J, Braun-Fahrlander C, Bolte J, Egger M, Roösli, M. Temporal and spatial variability of personal exposure to radiofrequency electromagnetic fields. Environmental Research (109):779–785; 2009.

Helsel DR. In: Scott M, Barnett V, editors. Nondetects and data analysis. New Jersey: John Wiley & Sons Inc; 2005.

International Commission on Non-Ionizing Radiation Protection. Guidelines for limiting exposure to time-varying electric, magnetic, and electromagnetic fields (up to 300 GHz). Health Physics 74: 494-522; 1998.

Iskra S, McKenzie R, Cosic I. Monte Carlo simulations of the electric field close to the body in realistic environments for application in personal radiofrequency dosimetry. Radiat Prot Dosimetry 147(4): 517-527; 2011.

Joseph W, Vermeeren G, Verloock L, Heredia MM, Martens L. Characterization of Personal RF Electromagnetic Field Exposure and Actual Absorption for the General Public. Health Physics 95(3):317-330; 2008.

Joseph W, Frei P, Roösli M, Thuróczy G, Gajsek P, Trcek T, Bolte J, Vermeeren G, Mohler E, Juhász P, Finta V, Martens L. Comparison of personal radio frequency electromagnetic field exposure in different urban areas across Europe. Environ Res. 110(7):658-63; 2010.

Kalliola K, Sulonen K, Laitinen H, Kivekäs O, Krogerus J, Vainikainen P. Angular power distribution and mean effective Gain of mobile antenna in different propagation environments. IEEE transactions on vehicular technology 51 (5): 823-838; 2002.

Knafl U, Lehmann H, and Riederer M. Electromagnetic field measurements using personal exposimeters. Bioelectromagnetics 29:160-162; 2008.

Lauer O, Neubauer G, Röösli M, Riederer M, Frei P, Mohler E, Fröhlich J.

Measurement Setup and Protocol for Characterizing and Testing Radio Frequency Personal Exposure Meters. Bioelectromagnetics 33: 75-85; 2012.

Neubauer G, Feychting M, Hamnerius Y, Kheifets L, Kuster N, Ruiz I, Schüz J, Uberbacher R, Wiart J, Röösli M. Feasibility of future epidemiological studies on possible health effects of mobile phone base stations. Bioelectromagnetics 28:224-230; 2007.

Neubauer G, Cecil S, Giczi W, Petric B, Preiner P, Fröhlich J, Röösli M. The association between exposure determined by radiofrequency personal exposimeters and human exposure: a simulation study. Bioelectromagnetics 31: 535-545; 2010.

Röösli M, Frei P, Mohler E, Braun-Fahrländer C, Burgi A, Fröhlich J, Neubauer G, Theis G, Egger M. Statistical analysis of personal radiofrequency electromagnetic field measurements with nondetects. Bioelectromagnetics 29(6):471-478; 2008.

Thielens A, De Clerq H, Agneessens S, Lecoutere J, Verloock L, Declerq F, Vermeeren G, Tanghe E, Rogier H, Puers R, Martens L, Joseph W. Distributed on Person Exposimeters for Radio Frequency Exposure Assessment in Real Environments. Bioelectromagnetics 34 (7): 563-567; 2013a.

Thielens A, Vermeeren G, Joseph W, Martens L. Stochastic Method for the Determination of the Organ-specific Averages SAR in Realistic Environments at 950 MHz. Bioelectromagnetics 34 (7): 549-562; 2013b.

Thielens A, Agneessens S, Verloock L, Tanghe E, Rogier H, Martens L, Joseph W. On-Body Calibration and Processing for a Combination of Two Radio Frequency Personal Exposimeters. Radiation Protection Dosimetry, published online: doi:10.1093/rpd/ncu056.

Vermeeren G, Joseph W, Olivier C, Martens L. Statistical multipath exposure of a human in a realistic electromagnetic environment, Health Physics 94: 345 – 54; 2008.

Vermeeren G, Joseph W, Martens L. Statistical multi-path exposure method for assessing the whole-body SAR in a heterogeneous human body model in a realistic environment, Bioelectromagnetics 34(3):240-251; 2013.

Viel JF, Cardis E, Moissonnier M, deSeze R, Hours M. Radiofrequency exposure in the French general population: Band, time, location and activity variability. Environ Int 35 (8): 1150-1154; 2009.

LIST OF CAPTIONS

Table 1: Weight factors (w_i), median on-body antenna apertures (AA_i), and detection limits (DLs) found for different combinations of the calibrated antennas for WiFi. The values are accompagnied by an uncertainty, estimated as half the interquartile distance over 100 bootstrap samples.

Table 2: Summary statistics after ROS and percentage of censored power densities measured in Ghent along the trajectory shown in Fig. 3, together with the upper and lower limit of the interval of the uncertainty on the measured values in which 50% of the estimates are located.

Figure 1: Measured impedance matching of the antennas around the WiFi band. The blue curve indicates the magnitude of the reflection coefficient ($|S_{11}|$), while the green zone indicates the WiFi band.

Figure 2: On-body positions where the RF nodes are placed during calibration and measurements. The positions of the WiFi antennas are indicated by a green circle. The grey surface indicates all the positions at 1cm from the VFM. (a) Frontal view, (b) rear view.

Figure 3: Trajectory followed by the subject wearing the PDE in Ghent, Belgium (from Google maps, CA USA). The grey line indicates the trajectory.

Figure 4: Numerically determined Experimental Cumulative Distribution Function (ECDF) of the interquartile distance of a single textile antenna placed on the upper body,

compared to the interquartile distance of a (weighted) average of two antennas placed on the front and back of the torso.

Figure 5: Minimal 50% prediction interval on the antenna aperture measured during calibration for a realistic polarization and all combinations of 2 antennas using an arithmetic and geometric weighted average.

Combination of Nodes		WiFi	
		arithmetic	geometric
1	AA_1 (cm²)	1.3 ± 0.0	
	DL (nW/m²)	6.9 ± 0.0	
2	AA_2 (cm²)	1.2 ± 0.0	
	DL (nW/m²)	7.4 ± 0.0	
(1,2)	$AA^{av/geom}$ (cm²)	9.8 ± 0.0	1.7 ± 0.0
	weights (w_1, w_2)	(0.40,0.60) $\pm$0.01	(0.49,0.51) $\pm$0.01
	DL (nW/m²)	0.91 ± 0.00	5.2 ± 0.0

*AA_1 = antenna aperture of antenna 1, AA_2 = antenna aperture of antenna 2, DL = detection limit

$AA^{av/geom}$ = the arithmetic or geometric weighted averaged antenna aperture,

Table 1

S_{inc} (μW/m²)	Node	averaging	Censored data (%)	u_{low} (%)	u_{up} (%)	$\mu\ (S_{inc})$ (μW/m²)	$p_{25}(S_{inc})$ (μW/m²)	$p_{50}(S_{inc})$ (μW/m²)	$p_{75}(S_{inc})$ (μW/m²)
WiFi 2G									
	1		0.8 and 0.0	94	190	0.094	0.033	0.065	0.18
	2		0.0 and 0.0	94	1200	0.057	0.034	0.040	0.061
	(1,2)	geom		32	43	0.059	0.027	0.042	0.079
	2x PEM	arith	19 and 22	33	77	0.52	0.16	0.52	1.7

* $\mu\ (S_{inc})$, $p_{25}(S_{inc})$, $p_{50}(S_{inc})$, and $p_{75}(S_{inc})$ are the mean, 25%, 50% ,and 75% percentiles of the incident power densities measured during the walk.

Table 2

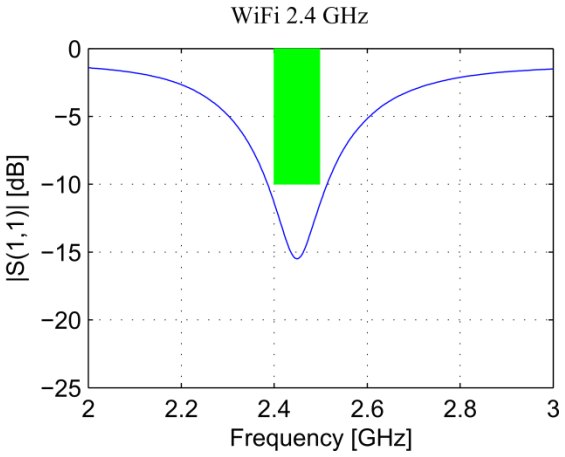

Fig. 1

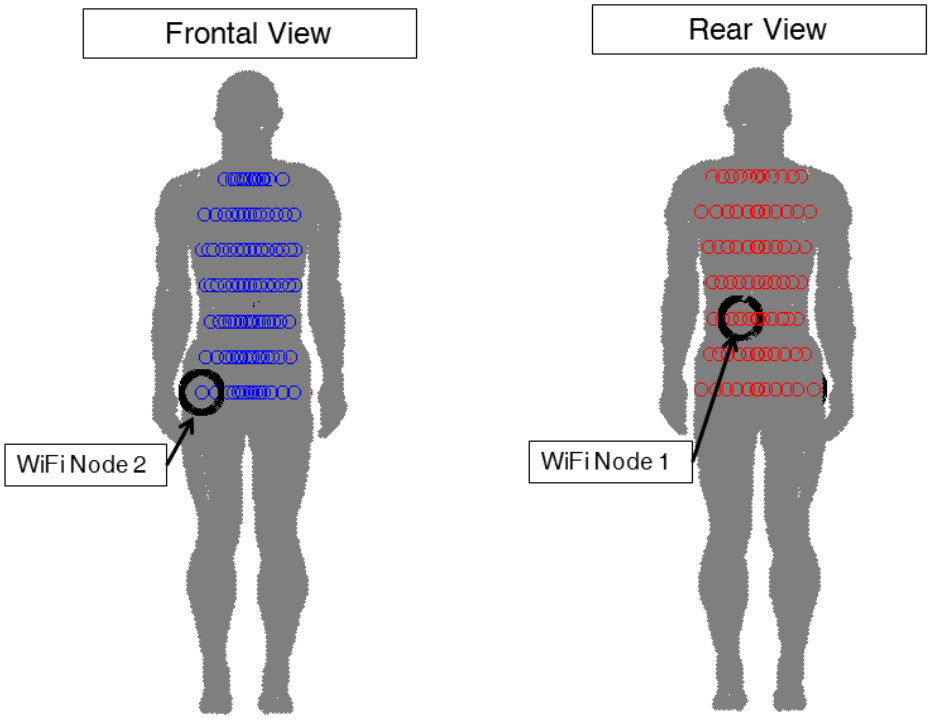

(a) (b)

Fig. 2

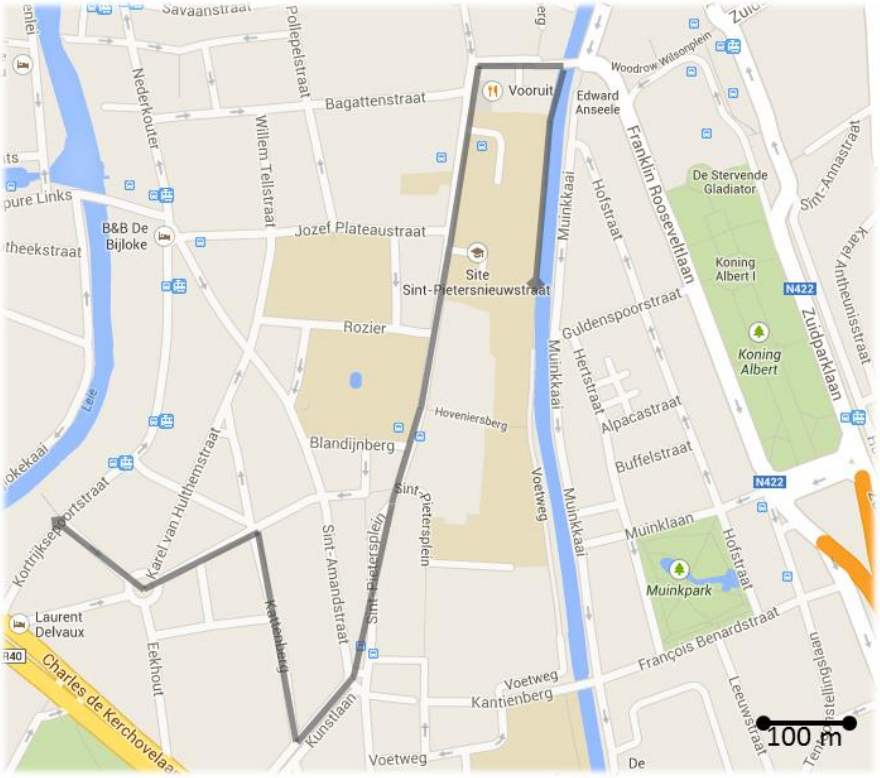
Savaanstraat
Pollepelstraat
Nederkouter
Bagattenstraat
Willem Tellstraat
Vooruit
Edward Anseele
Woodrow Wilsonplein
Franklin Rooseveltlaan
Muinkkaai
Hofstraat
De Stervende Gladiator
Sint-Annastraat
Karel Antheunisstraat
Koning Albert I
N422
Zuidparklaan
Koning Albert
Jozef Plateaustraat
B&B De Bijloke
Site Sint-Pietersnieuwstraat
Rozier
Guldenspoorstraat
Hertstraat
Alpacastraat
Buffelstraat
Hoveniersberg
Blandijnberg
Leie
Kortrijksepoortstraat
Karel van Huffelstraat
Sint-Amandstraat
Sint-Pietersplein
Voetweg
Muinklaan
Hofstraat
Muinkpark
Laurent Delvaux
Kantienberg
François Benardstraat
Eekhout
Charles de Kerchovelaan
Voetweg
Kantienberg
Kunstlaan
Leeuwstraat
Voetweg
100 m

Fig. 3

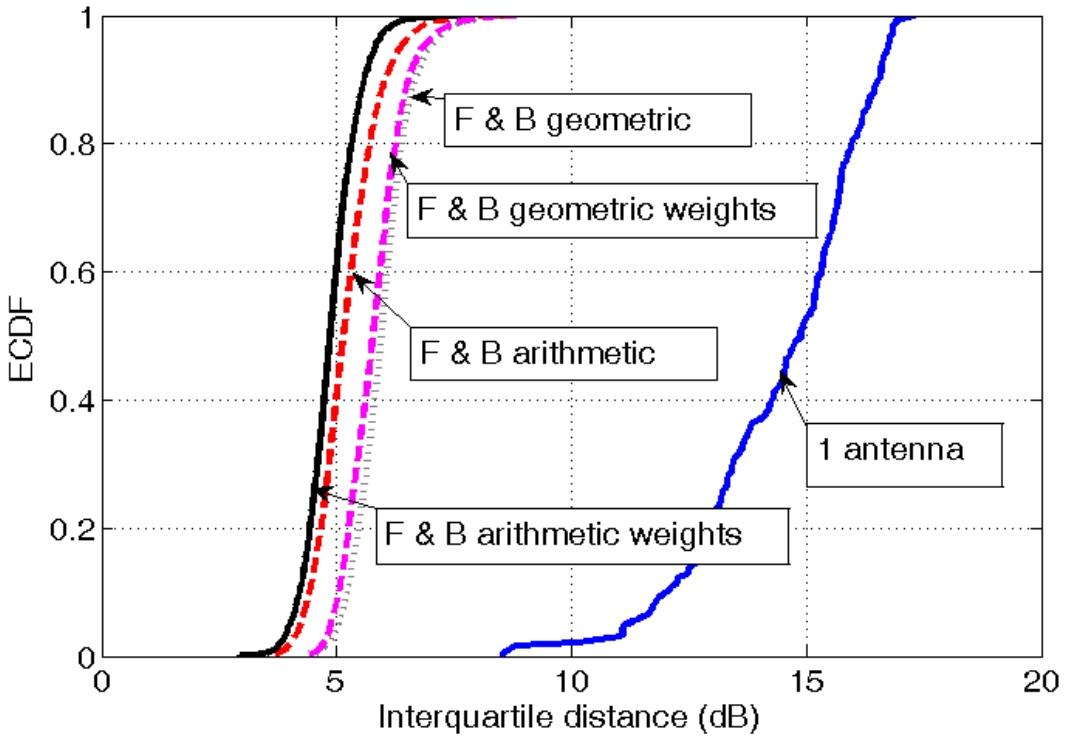
ECDF
Interquartile distance (dB)
F & B geometric
F & B geometric weights
F & B arithmetic
F & B arithmetic weights
1 antenna
0
0.2
0.4
0.6
0.8
1
0
5
10
15
20

Fig.4

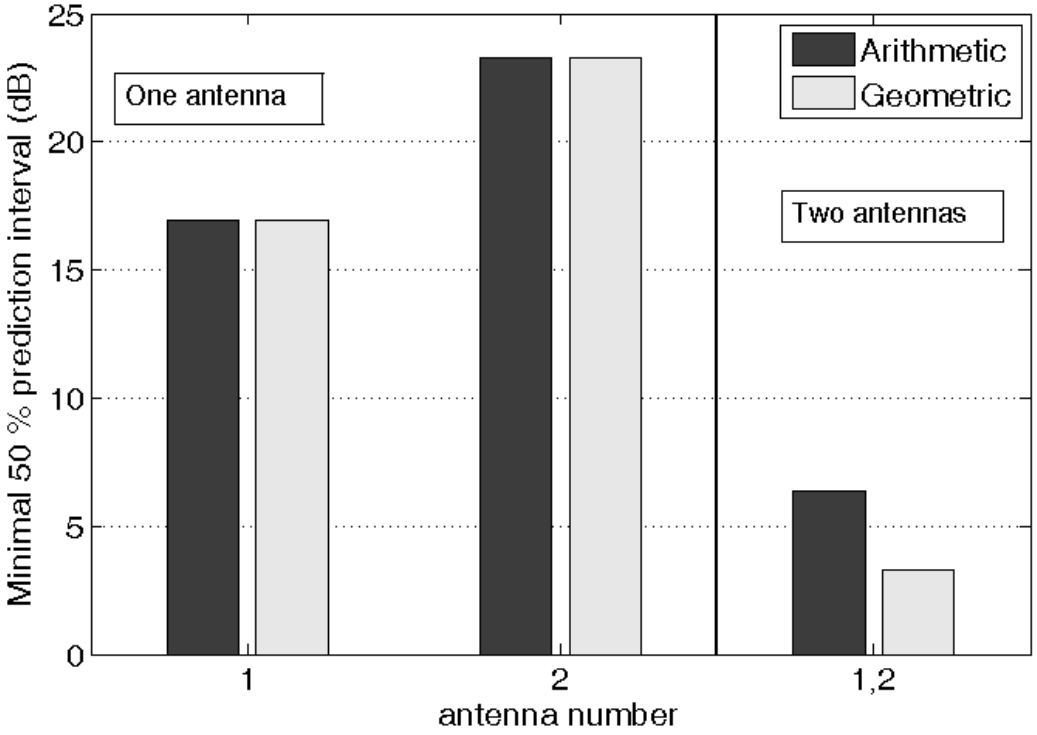
25
20
15
10
5
0
Minimal 50 % prediction interval (dB)
One antenna
Two antennas
Arithmetic
Geometric
1
2
1,2
antenna number

Fig.5